

# Experimental Results

*A. Bunyatyan, A. Cooper-Sarkar, C. Diaconu, R. Engel, C. Kiesling, K. Kutak, S. Ostapchenko, T. Pierog, T.C. Rogers, M.I. Strikman, T. Sako*

## 1 From HERA to LHC and Cosmic Rays

There seem to be two prime motivations for discussing HERA data in connection with the future running at the LHC and the physics of cosmic rays. First of all, HERA provides a precise picture of the structure of the proton, which are the scattering partners at the LHC. Concerning cosmic ray physics, the electron-proton ( $ep$ ) reactions at HERA can be viewed as collisions of ultra-high-energy photons - emitted by the electron - with nuclear matter. Comparing to the cosmic ray energy spectrum impinging on the earth's atmosphere, the HERA collider provides a photon beam equivalent to 50 TeV on a stationary proton target, lying about half way on a logarithmic scale, at about almost  $10^{14}$  eV, between the intensity maximum at 1 GeV and the "ankle" of the cosmic ray energy spectrum. Such high energy photon-proton collisions are of utmost importance for observational astrophysics, in particular for the understanding of the interactions of ultra-high-energy cosmic photons with our atmosphere which usually serves as the target in the cosmic ray experiments.

High energy photon interactions with hadronic matter are governed mainly by the strong interaction, which can be successfully described by quantum chromodynamics (QCD) as long as some "hard scale" of order several GeV is present in the reactions under study. Owing to the photon in the initial state, the overall size of the cross sections, however, is small, being proportional to the square of the fine-structure constant  $\alpha$ . In view of the LHC, the HERA data give direct information on quantities related to QCD, most importantly the parton distribution functions (pdfs) within the nucleon, and the running strong coupling  $\alpha_s$ , determining the overall strength of the partonic branching processes. These quantities, among others, are important ingredients to the Monte Carlo programs simulating cosmic ray showers in the atmosphere. There is, however, another interesting area in cosmic ray research, where HERA can provide important information, namely ultra-high energy neutrino scattering, which can be inferred from  $ep \rightarrow \nu X$  reactions at HERA. Also here, the neutrino energy accessible at HERA is equivalent to about 50 TeV on a stationary proton target.

In the following we will briefly summarize the data on the total photoproduction cross section from HERA and present some recent results on inclusive scattering, discussing the extraction of the parton distribution functions from a combined data set of the two collider experiments H1 and ZEUS. We will then discuss jet final states with emphasis on the phase space near the forward (proton) direction. These data shed light on the parton evolution models and also enable a unique measurement of the running strong coupling, providing new insight into QCD dynamics at very low values of the Bjorken variable  $x$ . We finally mention the relevance of the HERA charged current cross sections for the expectation of ultra-high energy neutrino nucleon cross sections, which will be elaborated in more detail in section 3.

**The HERA Physics Mission** One of the most successful tools for unraveling the structure of hadrons, most importantly of the nucleons, is deep-inelastic scattering (DIS) using charged leptons as probes. The HERA collider at the Deutsches Elektronen-Synchrotron DESY in Hamburg has provided the highest available center-of-mass energies for the collision of electrons and positrons with protons. HERA has been running from 1992 until mid 2007, accumulating a total of about  $500 \text{ pb}^{-1}$  for each of the two colliding beam experiments H1 [1] and ZEUS [2]. The data taking was divided into two phases, separated by a massive luminosity upgrade program in the years 2001-2002. As a further benefit of the upgrade, HERA also provided longitudinally polarized electron and positron beams, giving access to sensitive tests of the electroweak theory and allowing to carry out unique searches for the production of new heavy particles. While the electroweak sector was tested in electron-quark scattering at an unprecedented level, the hope for discovering “New Physics” at HERA did not materialize.

**Photoproduction at HERA** Measuring the total hadronic photoproduction cross section at high center-of-mass energies gives access to the asymptotic behavior of cross sections in general. The energy dependences of the total cross sections for  $pp$ ,  $\bar{p}p$ ,  $Kp$  and  $\pi p$  are well described by Regge theory [3]. Phenomenological fits based on this (non-perturbative) theory are successfully parameterizing all the hadronic cross sections in the full energy range (above the  $s$ -channel resonance region) using the common form

$$\sigma_{\text{tot}} = A \cdot s^\epsilon + B \cdot s^{-\eta},$$

where  $s$  is the square of the center-of-mass energy and  $A$  and  $B$  are constants. The parameter  $\epsilon$  describes the weak energy dependence at high energies ( $1 + \epsilon$  is the “Pomeron intercept”, which is about 1.09).

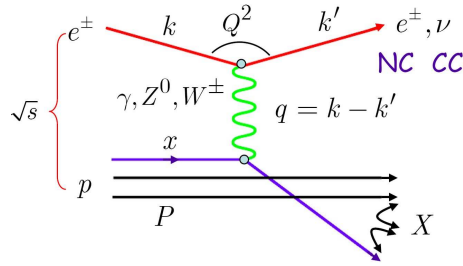


Fig. 1: Lowest order Feynman diagram for deep-inelastic electron-proton scattering in the parton picture, showing the relevant kinematic quantities characterizing inclusive DIS reactions and photoproduction (see text). The hadronic final state “fragmented” from the scattered and spectator partons is indicated by  $X$ .

The photon-proton total cross section is measured in the process  $ep \rightarrow e\gamma p \rightarrow eX$ , where the initial state electron has radiated a photon, which is then absorbed by the proton, producing a hadronic final state  $X$ . The event kinematics (see fig. 1 for a general lowest order Feynman diagram) is best described in terms of the Lorentz-invariant photon virtuality  $Q^2$ , and the event inelasticity  $y$ , both defined as

$$Q^2 = -q^2 = -(k - k')^2$$

and

$$y = \frac{p \cdot q}{p \cdot k}.$$

The square of the photon-proton center-of-mass energy  $W$ , i.e. the mass squared of the hadronic system  $X$ , is given by

$$W^2 = (q + p)^2 = 4E_e E_p y.$$

The photon virtuality has a kinematic minimum due to the finite electron mass  $m_e$ , and is given by

$$Q_{\min}^2 = \frac{m_e^2 y^2}{1 - y}.$$

The photoproduction cross section is related to the double differential electroproduction cross section (which is actually observed experimentally) by the equivalent photon approximation [4], which can be written as

$$\frac{d^2\sigma^{ep}}{dydQ^2} = \frac{\alpha}{2\pi Q^2} \left[ \left( \frac{1 + (1 - y)^2}{y} - \frac{2(1 - y)}{y} \frac{Q_{\min}^2}{Q^2} \right) \cdot \sigma_T^{\gamma p}(y, Q^2) + \frac{2(1 - y)}{y} \cdot \sigma_L^{\gamma p}(y, Q^2) \right],$$

where  $\sigma_T^{\gamma p}$  ( $\sigma_L^{\gamma p}$ ) is the cross section for transversely (longitudinally) polarized photon on protons. Since the virtuality of the photon is small by excluding deep inelastic scattering events ( $Q_{\max}^2 \sim 0.02 \text{ GeV}^2$ ), the longitudinal cross section is expected to be small. Integrating over  $Q^2$  gives the total  $\gamma p$  cross section in terms of the single  $ep$  differential cross section:

$$\sigma_{\text{tot}}^{\gamma p}(y) = \frac{2\pi}{\alpha} \left[ \frac{1 + (1 - y)^2}{y} \ln \frac{Q_{\max}^2}{Q_{\min}^2} - \frac{2(1 - y)}{y} \left( 1 - \frac{Q_{\min}^2}{Q_{\max}^2} \right) \right]^{-1} \cdot \frac{d\sigma^{ep}(y)}{dy}$$

The event inelasticity  $y$  is given by the acceptance of the electron tagging systems and can be integrated over, so that  $\sigma_{\text{tot}}^{\gamma p}(W)$  can be determined. The results of the measurements from HERA [5, 6] are shown in fig 2, together with the low energy data [7] and a phenomenological Regge fit [8] using hadron data, marked as “DL98”. The compatibility of the photoproduction cross section with the hadronic data supports the universal energy dependence of all total cross sections at asymptotic energies.

**Quantum Chromodynamics in the HERA Regime** Quantum Chromodynamics (QCD) is expected to describe the strong interactions between quarks and gluons. At distances small compared to the nucleon radius, or equivalently large momentum transfer  $Q^2$  where the strong coupling  $\alpha_s$  is small, perturbative QCD (pQCD) gives an adequate quantitative account of hadronic processes. The total cross sections, however, are dominated by long range forces (“soft interactions”), where a satisfactory understanding of QCD still remains a challenge. This is most importantly so also for all transitions of partons to hadrons in the final state (“fragmentation process”). In addition, non-perturbative effects govern the DIS kinematics through the momentum distribution (“parton distribution functions”, or “pdfs”) of the initial partons, interacting with the electrons via photon or  $Z^0$  exchange (see fig.1). The latter is important only at very large  $Q^2$ , i.e. around or beyond the mass of the  $Z^0$ . The division between the non-perturbative and the perturbative regimes is defined by the factorization scale, which should be sufficiently large ( $\mathcal{O}(\text{few GeV}^2)$ ) to hope for a convergent perturbative expansion in the strong coupling constant  $\alpha_s$ .

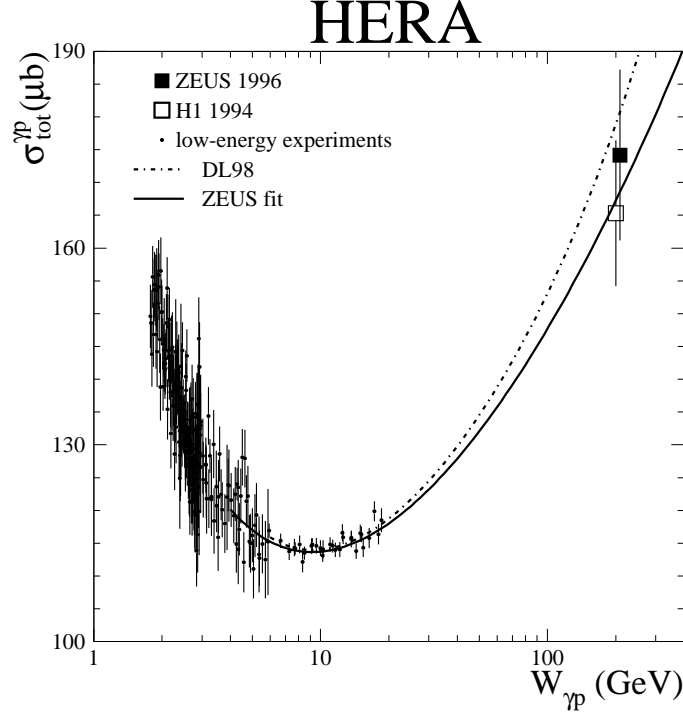


Fig. 2: Measurements of the total photoproduction cross section  $\sigma_{\gamma p}$  for positron-proton scattering from early measurements of H1 [5] and ZEUS [6].

Within the framework of perturbative QCD, the DIS cross section at the parton level is generically given by

$$\sigma = \sum_i \sigma_{\gamma^* i}(Q^2) \otimes x f_i(x, Q^2), \quad (1)$$

where  $Q^2$  is the virtuality of the exchanged boson (here: the virtual photon  $\gamma^*$ ),  $x$  is the momentum fraction (Bjorken  $x$ ) of the incoming parton, and  $\sigma_{\gamma^* i}$  is the total virtual photon-parton cross section. In this expression the factorization theorem of QCD [9] has been used, separating the cross section into a hard scattering part between the exchanged virtual photon and the incoming parton  $i$ , convoluted with a part (including a non-perturbative contribution) describing the momentum distribution  $x f_i(x, Q^2)$  of parton  $i$  within the proton. In eq.(1) one recognizes the incoherent summing of quark contributions, which is justified by the property of asymptotic freedom. Asymptotic freedom states that the interaction between the partons within the proton, characterized by the strong coupling constant  $\alpha_s$  become weak at large  $Q^2$  ( $\alpha_s \rightarrow 0$  as  $Q^2 \rightarrow \infty$ ). In this way the scattering process of the electron with the partons of the proton can be treated incoherently.

Figure 1 also indicates the kinematics in the HERA regime. Here,  $s$  is the square of the total  $ep$  center of mass energy. The four-momentum transfer squared  $Q^2$  is given by the scattered electron alone, the Bjorken variable  $x$  and the inelasticity  $y$  (equal to the energy fraction transferred from the electron to the virtual photon in the proton rest frame, see above), with  $x$

given by

$$x = \frac{Q^2}{2P \cdot q}. \quad (2)$$

Only two of the three quantities in eq. (2) are independent, they are related via  $Q^2 = sxy$ . Another interesting quantity is the total mass  $M_X$  of the hadronic final state, given by

$$M_X^2 \equiv W^2 = (q + P)^2 = \frac{Q^2(1-x)}{x} \quad (3)$$

This relation shows that low  $x$  reactions correspond, at fixed  $Q^2$ , to large values of  $W^2$ , i.e. large invariant masses of the hadronic final state. Due to the high colliding beam energies (protons at 920 GeV, electrons at 27.6 GeV), HERA provided a large range of exploration for  $x$  and  $Q^2$ , extending the reach of previous fixed target experiments by more than 2 orders of magnitude in  $x$  and  $Q^2$ .

The double differential cross section for  $ep$  scattering is written in terms of structure functions as (see, e.g. [10])

$$\frac{d^2\sigma(e^\pm p)}{dx dQ^2} = \frac{2\pi\alpha^2}{xQ^4} Y_+ \left[ F_2 - \frac{y^2}{Y_+} F_L \mp \frac{Y_-}{Y_+} xF_3 \right], \quad (4)$$

where the functions  $Y_\pm$  are given by  $Y_\pm = 1 \pm (1-y)^2$ , and the structure functions, apart from coupling constants, are combinations of the parton distribution functions. For the case of pure photon exchange, valid at low  $Q^2$ , one obtains

$$F_2(x, Q^2) = \sum_{i=u,d,\dots} e_i^2 x f_i(x, Q^2). \quad (5)$$

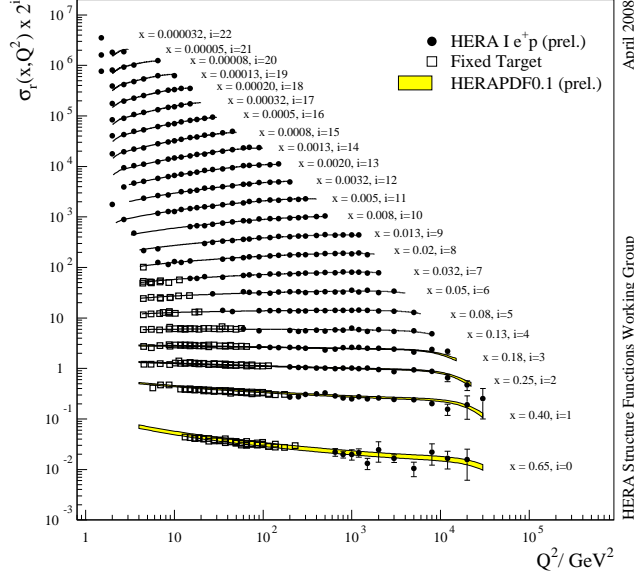
where the sum extends over all partons within the proton of charge  $e_i$ . As indicated in fig. 1, all reactions with neutral boson exchange are called “neutral current (NC)” reactions, those with  $W^\pm$  exchange (here the final state lepton is a neutrino) are called “charged current (CC)” reactions.

The non-perturbative parton distribution functions  $f_i(x)$  cannot be calculated from first principles and have therefore to be parameterized at some starting scale  $Q_0^2$ . Perturbative QCD predicts the variation of  $f_i$  with  $Q^2$ , i.e.  $f_i = f_i(x, Q^2)$  via a set of integro-differential evolution equations, as formulated by Altarelli and Parisi (“DGLAP” equations, see [11]). The predicted  $Q^2$  dependence (“scaling violations”) of the structure function  $F_2$ , see eq. (5), are nicely supported by the data from HERA [12].

**Low  $x$  Physics and the Parton Distribution Functions** At distances small compared to the nucleon radius, or equivalently large momentum transfer  $Q^2$  between the incoming and outgoing leptons, perturbative QCD (pQCD) gives an adequate quantitative account of hadronic processes in DIS. The most “elementary” observable in electron-proton scattering is the inclusive DIS cross section, where basically only the 4-vectors of the scattered lepton or the produced hadronic final state are measured.

Inclusive  $ep$  scattering can be divided into two distinct classes: Neutral current (NC) reactions ( $ep \rightarrow eX$ ), and Charged Current (CC) reactions ( $ep \rightarrow \nu X$ ). In NC reactions, a photon or

### H1 and ZEUS Combined PDF Fit



April 2008

HERA Structure Functions Working Group

Fig. 3: Measurements of the reduced cross section  $\sigma_r(x, Q^2)$  for positron-proton scattering, based on the combined data of H1 and ZEUS [12]. The data show clear evidence for scaling violations, as expected from gluon emission of the initial quarks participating in the hard scattering process. The scaling violations are very well described by pQCD NLO fit HERAPDF 0.1 [13]. At low  $Q^2$ , the data from some fixed target experiments are also shown.

a  $Z^0$  is exchanged between the electron and a quark emitted from the proton. The corresponding double-differential cross section  $d^2\sigma/dxdQ^2$ , or the so-called “reduced” cross section  $\sigma_r$  factorizing out known kinematic terms, can be written in the following way (similar expressions also hold for the CC reactions):

$$\sigma_r(x, Q^2) \equiv \left( \frac{xQ^4}{2\pi\alpha^2 Y_+} \right) \frac{d^2\sigma(e^\pm p)}{dx dQ^2} = F_2 - \frac{y^2}{Y_+} F_L \mp \frac{Y_-}{Y_+} xF_3 \quad (6)$$

Here, the three (positive definite) structure functions  $F_2$ ,  $F_L$  and  $xF_3$  depend both on  $x$  and  $Q^2$ , and contain the (non-perturbative) parton distribution functions (pdfs). The structure function  $F_2$  contains contributions from quarks and antiquarks ( $\sim x(q + \bar{q})$ ),  $F_L$  is dominated by the gluon distribution ( $\sim xg$ ), and  $xF_3$  is sensitive to the valence quarks ( $\sim x(q - \bar{q})$ ).

At low  $Q^2$  and low  $y$  the structure functions  $xF_3$  (from  $Z^0$  exchange) and  $F_L$  (suppressed by the factor  $y^2$ ) can be safely neglected. Residual (small) contributions from  $F_L$  can also be modeled using pQCD. In this case the structure function  $F_2$  can be extracted at each point of  $x$  and  $Q^2$  from the “reduced” cross section  $\sigma_r$  (see eq. (6)). Measurements of  $\sigma_r$  from the combined H1 and ZEUS data [12] are shown in fig. 3. The data, most importantly their  $Q^2$  dependence, are very well described by NLO pQCD.

Figure 4 shows the pdfs resulting from the NLO pQCD fit HERAPDF 0.1 to the combined NC and CC double-differential cross sections from both HERA experiments [13]. The

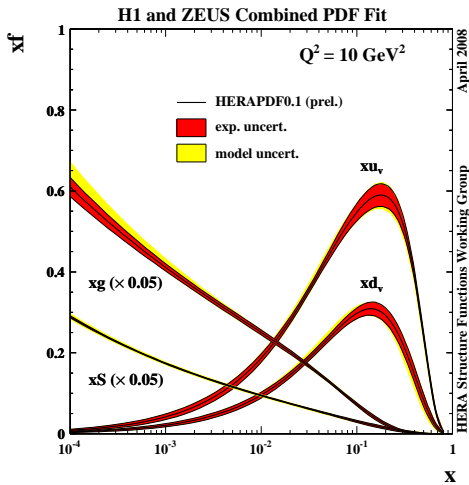


Fig. 4: The parton distribution functions from QCD fits to the HERA data on NC and CC inclusive reactions, using the combined data from H1 and ZEUS (HERAPDF 0.1) [13].

resulting uncertainties of the pdfs have drastically shrunk due to the combination of the HERA data. It should also be noted that the pdfs for the gluon and the sea quarks, even at the lowest values of Bjorken  $x$ , and for all values of  $Q^2$ , keep rising with decreasing  $x$ . This means that parton saturation has not been observed within the kinematic range of HERA - assuming that the parameterisation used in the fits would be flexible enough to allow the observation of such behaviour.

From fig. 4 one clearly sees that the gluon distribution is dominating the low  $x$  behavior of the DIS cross sections. At low  $x$ , the structure function  $F_2$  can be satisfactorily parameterized as being proportional to  $x^{-\lambda}$ . Figure 5 shows the values of  $\lambda$  as function of  $Q^2$ . One can observe a clear decrease of  $\lambda$  with decreasing  $Q^2$ , touching the hadron-hadron limit (and also photoproduction, see the left-most data point) at a photon virtuality around  $1 \text{ GeV}^2$ .

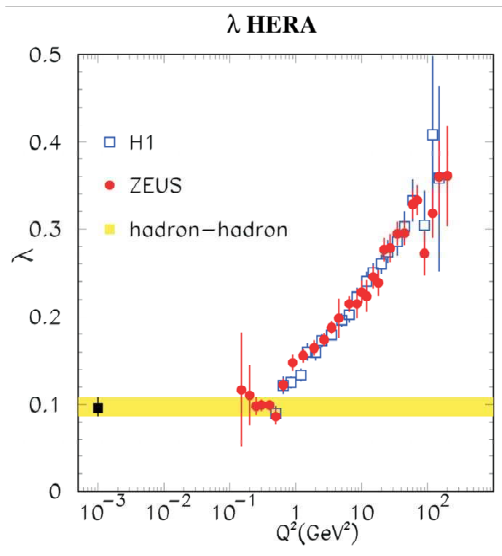


Fig. 5: Measurements of the slope of  $F_2$  for deep inelastic scattering as function of  $Q^2$ . To the far left, the photoproduction point  $\epsilon \equiv \lambda$  is also drawn.

**Jet Production** Collimated bundles of particles (“jets”) are carrying the kinematic information of the partons emerging from DIS reactions at HERA and other high  $p_t$  colliding beam experiments. The study of jet production is therefore a sensitive tool to test the predictions of perturbative QCD and to determine the strong coupling constant  $\alpha_s$  over a wide range of  $Q^2$ .

Several algorithms exist to cluster individual final state hadrons into jets, but most commonly used at HERA is the so-called  $k_T$  clustering algorithm [14]. The jet finding is usually executed in the hadronic center of mass system, which is, up to a Lorentz boost, equivalent to the Breit frame. At the end of the algorithm, the hadrons are collected into a number of jets.

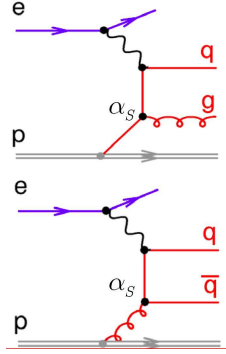


Fig. 6: Feynman diagrams for LO jet production. The upper subgraph is called “QCD Compton”, the lower subgraph is called “boson-gluon fusion”. Both graphs contribute to two-jet final states. Events with three jets can be interpreted as a di-jet process with additional gluon radiation from one of the involved quark lines, or as a gluon splitting into a quark-antiquark pair. These processes are of order  $\mathcal{O}(\alpha_s^2)$  (NLO).

At leading order (LO) in  $\alpha_s$ , di-jet production (see fig. 6) proceeds via the QCD Compton process ( $\gamma^* q \rightarrow qg$ ) and boson-gluon fusion ( $\gamma^* g \rightarrow q\bar{q}$ ). The cross section for events with three jets is of  $\mathcal{O}(\alpha_s^2)$ . These events can be interpreted as coming from a di-jet process with additional gluon radiation or gluon splitting (see caption of fig. 6), bringing the QCD calculation to next-to-leading order (NLO).

In jet physics, two different “hard” scales can be used to enable NLO (and higher) calculations: the variable  $Q$ , and the transverse energy  $E_T$  of the jets. Figure 7 shows the differential cross sections for inclusive jet production at high  $Q^2$  as measured by the ZEUS Collaboration [15], both with respect to  $Q^2$  and  $E_T$ . The data are compared to NLO calculations, using the renormalization and factorization scales as indicated in the figure. Both schemes are able to describe the data very well, indicating the validity of the choice of any of the two hard scales. Given the experimental and theoretical uncertainties at these large scales, no higher order (beyond NLO) corrections seem necessary.

**Forward Jets** All of the analyses regarding the observables mentioned in the previous chapters rest on the DGLAP  $Q^2$  evolution scheme for the pdfs involved. Potential deviations observed in certain regions of phase space (low  $x$ , low  $Q^2$ ) are usually attributed to the limited order of the presently computed QCD matrix elements (LO, NLO, sometimes NNLO). Especially for low  $x$  ( $\approx 10^{-4}$ ), but sufficiently large  $Q^2$  ( $>$  a few  $\text{GeV}^2$ ), there has been a vivid debate about the validity of the DGLAP approach. In this kinematic regime the initial parton in the proton can induce a QCD cascade, consisting of several subsequent parton emissions, before eventually an interaction with the virtual photon takes place (see fig. 8). QCD calculations based on the “direct” interaction between a point-like photon and a parton from the evolution chain, as given



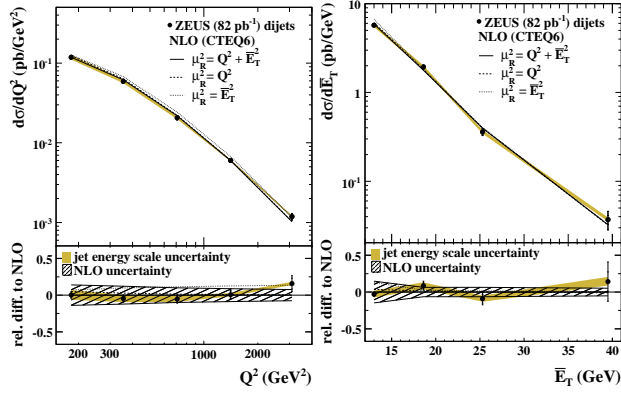


Fig. 7: Differential cross sections for inclusive jet production from the ZEUS experiment [15]. Also shown are the predictions from next-to-leading order QCD calculations, which give a good description of the data.

by the DGLAP approach, are very successful in describing, e.g. the unexpected rise of  $F_2$  with decreasing  $x$  over a large range in  $Q^2$  [16].

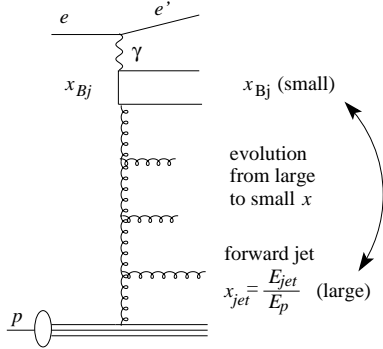


Fig. 8: Schematic diagram of  $ep$  scattering producing a forward jet. The evolution in the longitudinal momentum fraction  $x$ , from large  $x_{jet}$  to small  $x_{Bj}$ , is indicated.

For low values of  $x$ , there is, however, a technical reason to question the validity of the DGLAP evolution approach: Since it resums only leading  $\log(Q^2)$  terms, the approximation may become inadequate for very small  $x$ , where  $\log(1/x)$  terms become important in the evolution equations. In this region the BFKL scheme [17] is expected to describe the data better, since in this scheme terms in  $\log(1/x)$  are resummed.

The large phase space available at low  $x$  (see eq.(3)) makes the production of forward jets (in the angular region close to the proton direction) a particularly interesting topic for the study of parton dynamics, since jets emitted in this region lie well away in rapidity from the photon end of the evolution ladder (see fig. 8). Concerning the forward jets there is a clear dynamic distinction between the DGLAP and BFKL schemes: In the DGLAP scheme, the parton cascade resulting from hard scattering of the virtual photon with a parton from the proton is ordered in parton virtuality. This ordering along the parton ladder implies an ordering in transverse energy  $E_T$  of the partons, so that the parton participating in the hard scatter has the highest  $E_T$ . In the BFKL scheme there is no strict ordering in virtuality or transverse energy. The BFKL evolution therefore predicts that a larger fraction of low  $x$  events will contain high- $E_T$  forward jets than is predicted by the DGLAP evolution.

Both ZEUS [18] and H1 [19] have studied forward jet production, where “forward” typically means polar emission angles less than about 20 degrees relative to the proton direction. As

a first example, the single differential cross sections  $d\sigma/dx$  from H1 are shown in fig. 9. The data are compared to LO and NLO QCD calculations [20] (a), and several Monte Carlo models (b and c). The NLO calculation in (a) is significantly larger than the LO calculation. This reflects the fact that the contribution from forward jets in the LO scenario is kinematically suppressed. Although the NLO contribution opens up the phase space for forward jets and considerably improves the description of the data, it still fails by a factor of 2 at low  $x$ . In fig. 9b the predictions from the CASCADE Monte Carlo program [21] is shown, which is based on the CCFM formalism [22]. The CCFM equations provide a bridge between the DGLAP and BFKL descriptions by resumming both  $\log(Q^2)$  and  $\log(1/x)$  terms, and are expected to be valid over a wider  $x$  range. The model predicts a somewhat harder  $x$  spectrum, and fails to describe the data at very low  $x$ . In part (c) of the figure, the predictions (“RG-DIR”) from the LO Monte Carlo program RAPGAP [23] is shown, which is supplemented with initial and final state parton showers generated according to the DGLAP evolution scheme. This model, which implements only direct photon interactions, gives results similar to the NLO calculations from part (a), and falls below the data, particularly at low  $x$ . The description is significantly improved, if contributions from resolved virtual photon interactions are included (“RG-DIR+RES”). However, there is still a discrepancy in the lowest  $x$  bin, where a possible BFKL signal would be expected to show up most prominently. The Color Dipole Model (CDM) [24], which allows for emissions non-ordered in transverse momentum, shows a behavior similar to RG-DIR+RES.

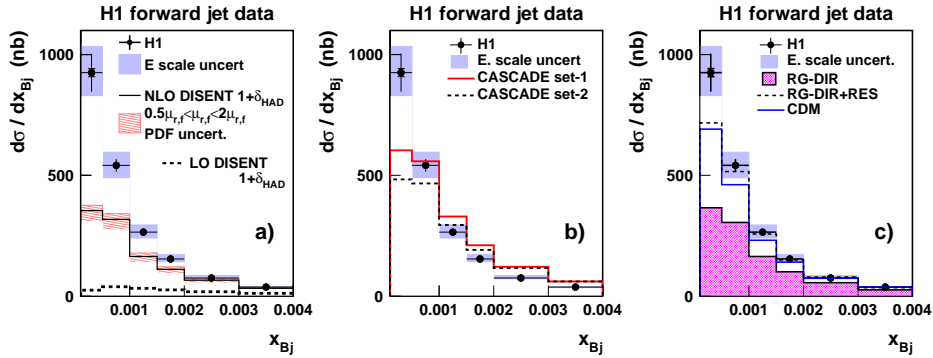


Fig. 9: Single differential cross sections for forward jets as functions of  $x$  from the H1 experiment [19], compared to NLO predictions [20] in (a), and QCD Monte Carlo models [23, 24] in (b) and (c). The dashed line in (a) shows the LO contribution.

For a more detailed study the forward jet sample was divided into bins of  $p_{t,\text{jet}}^2$  and  $Q^2$ . The triple differential cross section  $d^3\sigma/dx dQ^2 dp_{t,\text{jet}}^2$  versus  $x$  is shown in fig. 10 for several regions in  $Q^2$  and  $p_{t,\text{jet}}^2$ . In addition, the expectations from the above mentioned QCD models are presented. Using the ratio  $r = p_{t,\text{jet}}^2/Q^2$ , various regimes can be distinguished: For  $p_{t,\text{jet}}^2 < Q^2$  ( $r < 1$ ) one expects a DGLAP-like behavior, dominated by direct photon interactions (see fig. 10 c). Due to the large bin sizes, however, the ranges of  $r$  can be quite large, so that  $r$  in this bin can assume values up to 1.8 due to admixtures from events with  $p_{t,\text{jet}}^2 > Q^2$ . This may explain why the DGLAP direct model (RG-DIR), although closer to the data in this bin than in any other, does not quite give agreement with the data except at the highest  $x$ -bin. In the region

$p_{t,\text{jet}}^2 \approx Q^2$  ( $r \approx 1$ , see fig. 10 b and f), DGLAP suppresses parton emission, so that BFKL dynamics may show up. However, the DGLAP resolved model (RG-DIR+RES) describes the data reasonably well.

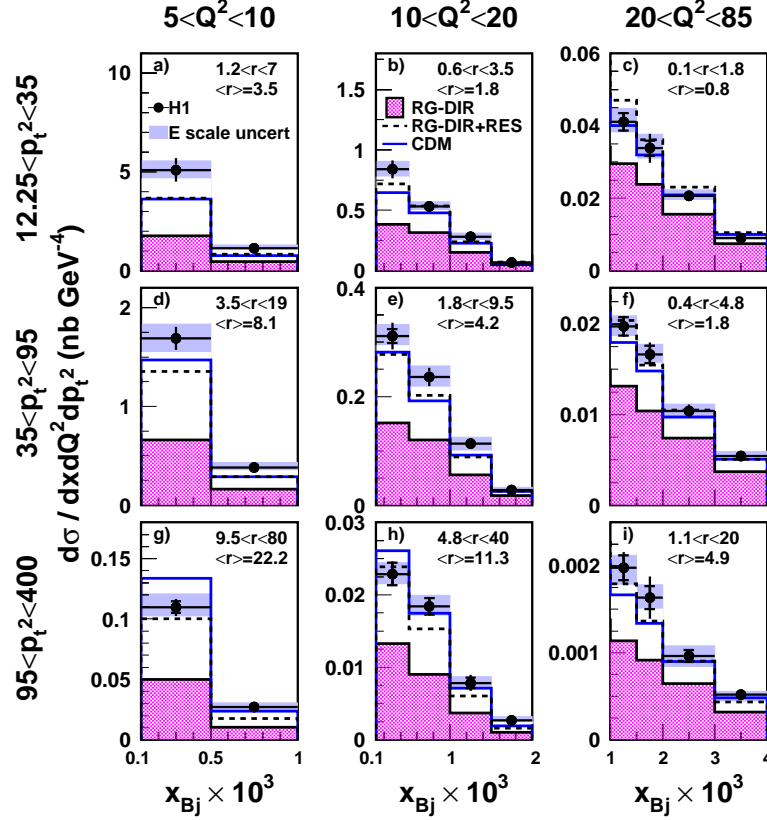


Fig. 10: Triple differential cross sections for forward jet production as function of  $x$  in bins of  $Q^2$  and  $p_{t,\text{jet}}^2$ , compared to various Monte Carlo calculations (see text).

The regime of  $p_{t,\text{jet}}^2 > Q^2$  ( $r > 1$ , see fig. 10 d, g and h), is typical for processes where the virtual photon is resolved, i.e. the incoming parton from the proton vertex interacts with a parton from the photon. As expected, the DGLAP resolved model (RG-DIR+RES) provides a good overall description of the data, again similar to the CDM model. However, it can be noted that in regions where  $r$  is largest and  $x$  is small, CDM shows a tendency to overshoot the data. DGLAP direct (RG-DIR), on the other hand, gives cross sections which are too low. Although the above analysis tries to isolate “BFKL regions” from “DGLAP regions”, the conclusion on underlying dynamics cannot be reached, most importantly since the “BFKL region” ( $r \approx 1$ ) is apparently heavily contaminated by “DGLAP-type” events. In addition, the two “different” evolution approaches, RG-DIR+RES (“DGLAP”) and CDM (“BFKL”), give similar predictions.

In a further step, the parton radiation ladder (see fig. 8) is examined in more detail by looking also at jets in the region of pseudorapidity,  $\eta = -\ln \tan(\theta/2)$ , between the scattered electron ( $\eta_e$ ) and the forward jet ( $\eta_{\text{forw}}$ ). In this region a “2-jet + forward” sample was selected,

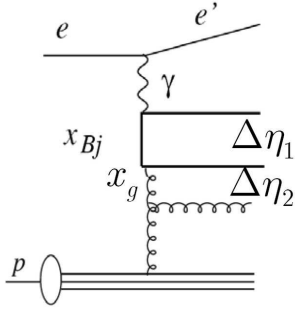


Fig. 11: Kinematic regions for the event sample “2jets + forward” (see text). The quarks in the photon-gluon fusion process are  $q_1$  (upper solid line) and  $q_2$  (lower solid line). The rapidity gap between  $q_1$  and  $q_2$  is denoted by  $\Delta\eta_1$ , the gap between  $q_2$  and the forward jet is denoted by  $\Delta\eta_2$ .

requiring at least 2 additional jets, with  $p_{t,\text{jet}} > 6$  GeV for all three jets, including the forward jet. In this scenario, evolution with strong  $k_t$  ordering is obviously disfavored. The jets are ordered in rapidity according to  $\eta_{\text{forw}} > \eta_{\text{jet}2} > \eta_{\text{jet}1} > \eta_e$ . Two rapidity intervals are defined between the two additional jets and the forward jet (see fig. 12):  $\Delta\eta_1 = \eta_{\text{jet}2} - \eta_{\text{jet}1}$  is the rapidity interval between the two additional jets, and  $\Delta\eta_2 = \eta_{\text{forw}} - \eta_{\text{jet}2}$  is the interval between jet 2 and the forward jet. If the di-jet system originates from the quark line coupling to the photon (see fig. 12), the phase space for evolution in  $x$  between the di-jet system and the forward jet is increased by requiring that  $\Delta\eta_1$  is small and that  $\Delta\eta_2$  is large: Requiring  $\Delta\eta_1 < 1$  will favor small invariant masses of the di-jet system. As a consequence,  $x_g$  will be small, leaving the rest for additional radiation. When, on the other hand,  $\Delta\eta_1$  is required to be large ( $\Delta\eta_1 > 1$ ) BFKL-like evolution may then occur between the two jets from the di-jet system or, when both  $\Delta\eta_1$  and  $\Delta\eta_2$  are small, between the di-jet system and the hard scattering vertex. Note that the rapidity phase space is restricted only for the forward jet.

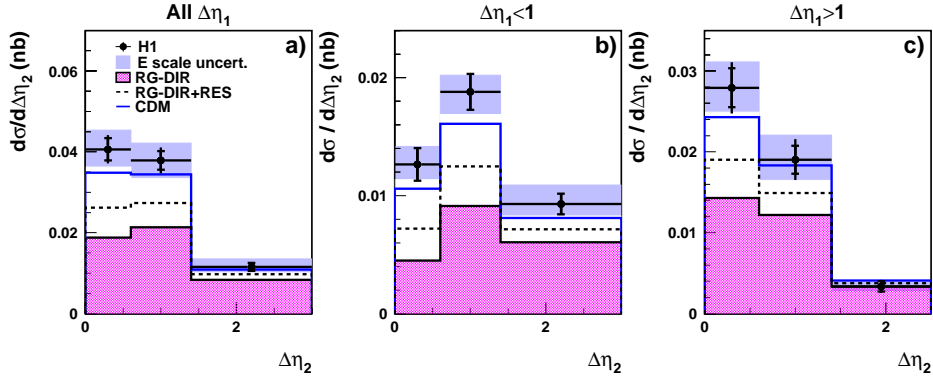


Fig. 12: Cross section for events with a reconstructed high transverse momentum di-jet system and a forward jet from the H1 experiment [19], as function of  $\Delta\eta_2$  for two regions of  $\Delta\eta_1$ . The data are compared to predictions of “DGLAP-like (RG-DIR+RES) and “BFKL-like” (CDM) Monte Carlo models (see text).

As argued above, this study disfavors evolution with strong ordering in  $k_t$  due to the common requirement of large  $p_{t,\text{jet}}$  for the three jets. Radiation which is not ordered in  $k_t$  may occur at any location along the evolution chain, depending on the values of  $\Delta\eta_1$  and  $\Delta\eta_2$ . Figure 12 show the measured cross sections as function of  $\Delta\eta_2$  for all data, and separated into the two regions of  $\Delta\eta_1$  discussed above. One can see that here the CDM model is in good agreement with

the data in all cases, while the DGLAP models predict cross sections which are too low, except when both  $\Delta\eta_1$  and  $\Delta\eta_2$  are large. For this topology all models (and the NLO calculation, not shown) agree with the data, indicating that the available phase space for evolution is exhausted.

It is important to realize that the “2+forward jet” sample indeed seems to differentiate between the CDM and DGLAP resolved models, in contrast to the more inclusive samples (see fig. 10). The conclusion is that additional breaking of the  $k_t$  ordering, beyond what is included in the resolved photon model, is required by the data, pointing towards some evidence for BFKL dynamics. It is, however, not excluded that such effects may also be described by higher order DGLAP calculations, which may become available in the future. Further investigations using forward particle emission will be discussed below (see section 2).

**The Strong Coupling Constant** One of the most important measurements using multi-jet final states is the determination of the strong coupling constant  $\alpha_s$ . At HERA, this measurement is particularly interesting, since  $\alpha_s$  can be determined in a single experiment over a large range of  $Q$  or  $E_T$ . Observables which are sensitive to  $\alpha_s$  come from various sources, such as inclusive jets, jet ratios (number of three jets relative to the number of two jets), and event shape variables (thrust, jet masses, angles between jets etc.). A recent compilation of  $\alpha_s$  determinations [25] from the two HERA experiments H1 and ZEUS, using various jet observables and the HERA I data set, is shown in fig. 13. An NLO fit to these data yields a combined value of  $\alpha_s(M_Z) = 0.1198 \pm 0.0019(\text{exp.}) \pm 0.0026(\text{th.})$ . The dominating theoretical error arises from the uncertainty due to terms beyond NLO, which is estimated by varying the renormalization scale by the “canonical” factors 0.5 and 2. A recent preliminary result obtained by the H1 Collaboration using the full HERA data set and based on multiple observables in inclusive and multi-jet events displays an experimental error below 1% [26]:  $\alpha_s = 0.1182 \pm 0.0008(\text{exp})_{-0.0031}^{+0.0041}(\text{th.}) \pm 0.0018$ . This illustrates the potential for a very precise measurement of the strong coupling using the full HERA data set.

**Ultra-High Energy Neutrino Reactions** With the era of high energy neutrino astrophysics approaching, it is interesting to review our knowledge about the neutrino-nucleon cross section at ultra-high energies beyond  $\mathcal{O}(10 \text{ TeV})$ . Such energies can indeed be reached with the HERA collider, as was discussed in the introduction. Looking at the charged current reaction  $ep \rightarrow \nu X$  measured at HERA, a cut in the transverse neutrino momentum of  $p_\perp > 25 \text{ GeV}$  is necessary for a clean separation of CC events from the background. The extrapolation to  $p_\perp = 0$  can be done within the Standard model, yielding a cross section for  $\nu N$  on a stationary target of about 200 pb at 50 TeV neutrino energy. Figure 14 shows the measurements from fixed target experiments and the HERA point. Also given are the linear extrapolation (corresponding to  $M_W = \infty$ ) and the prediction of the Standard Model ( $M_W = 80 \text{ GeV}$ ). As one can see, the neutrino nucleon cross section shows no anomaly, as could, for example, be expected by electroweak instanton effects proposed [27] as a source of possible cosmic ray events beyond the GZK cutoff. While the evidence for such events has become weaker recently [28,29], the search for instanton effects at HERA [30] has also been inconclusive so far. More details on the expectations of neutrino cross sections at asymptotic energies are presented further below (see section 3).

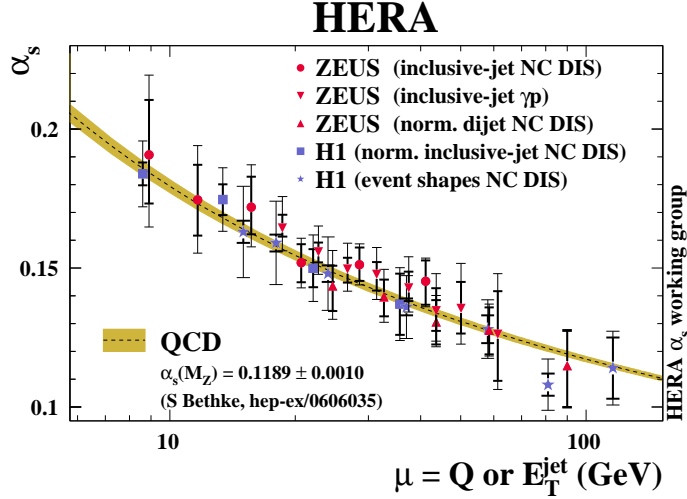


Fig. 13: Compilation of  $\alpha_s(\mu)$  measurements from H1 and ZEUS [25], based on jet variables as indicated. The dashed line shows the two loop solution of the renormalization group equation, evolving the 2006 world average for  $\alpha_s(M_Z)$ . The band denotes the total uncertainty of the prediction.

## 2 Forward particles from HERA to LHC

**Forward Particles at HERA** In  $ep$  scattering at HERA, a significant fraction of events contains a low-transverse momentum baryon carrying a large fraction of the incoming proton energy. Although the production mechanism of these leading baryons is not completely understood, exchange models [31] give a reasonable description of the data (Fig. 15). In this picture, the incoming proton emits a virtual particle which undergoes the deep inelastic scattering process with the incoming beam electron.

To measure the very forward particles, both the H1 and the ZEUS experiments have been equipped with the Forward Proton Spectrometers (LPS, FPS and VFPS) and the Forward Neutron Calorimeters (FNC). The Forward Proton Spectrometers are several Roman Pot detectors placed at different positions along the beamline in the direction of proton beam, between 24 and 220 m from the interaction point. They measure the energy and momentum of the protons which are scattered through the very small angles and keep a momentum fraction of the initial proton between 0.4 and 1.

The Forward Neutron Calorimeters were installed at  $\theta = 0^\circ$  and at 106 m from the interaction point in the proton beam direction. These are lead-scintillator sandwich calorimeters with energy resolution  $\sigma(E)/E = 70\%/\sqrt{E}$  for the ZEUS-FNC and  $\sigma(E)/E = 63.4\%/\sqrt{E} \oplus 3\%$  for the H1-FNC. The size and weight of the FNC are defined by the space available in the HERA tunnel. The detectors are about 2m long with  $\sim 70 \times 70 \text{ cm}^2$  transverse size. Below the H1 and ZEUS-FNC calorimeters are briefly described.

The general view of the H1-FNC is shown in Fig. 16(left). It consists of the Main Calorimeter and the Preshower. In addition, two layers of veto counters situated at the distance of 2m in front of Preshower are used to veto charged particles. The Preshower is  $\sim 40\text{cm}$  ( $\sim 1.5\lambda$ )

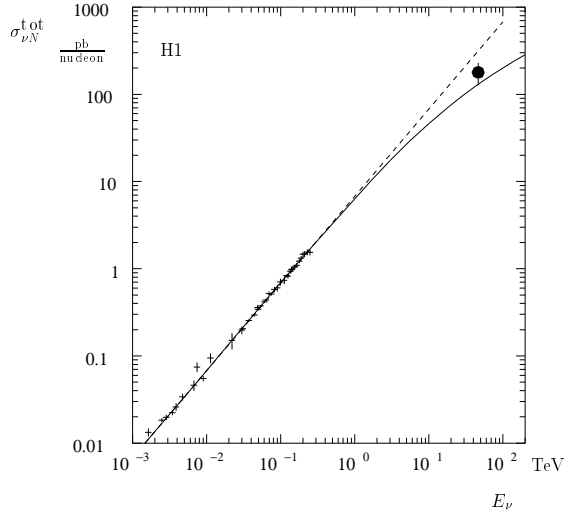


Fig. 14: Measurement of the neutrino nucleon total cross section inferred from the HERA charged current data (full circle), and various fixed target neutrino experiments (crosses).

long lead–scintillator sandwich calorimeter, it is placed in front of the Main Calorimeter. The electromagnetic showers completely develop in Preshower, while the hadronic showers leave in Preshower  $\sim 40\%$  of their energy (electromagnetic component). So the position resolution for the showers started in Preshower are defined by the electromagnetic component of the shower. Constructively the Preshower consists of two sections: the electromagnetic and the hadronic ones, each of them is composed of 12 planes. The transverse size of the scintillating plates is  $26 \times 26 \text{ cm}^2$ . Each scintillating plate has 45 grooves where 1.2mm wavelength shifters are glued in. In order to obtain a good spatial resolution, the orientation of fibres is changed in turn from horizontal to vertical for alternating planes. On each plate the fibres are combined by five into nine strips. Longitudinally the strips are combined in 9 vertical and 9 horizontal towers. The energy resolution for electromagnetic showers is  $\sim 20\%/\sqrt{E [\text{GeV}]}$  and the spatial resolution

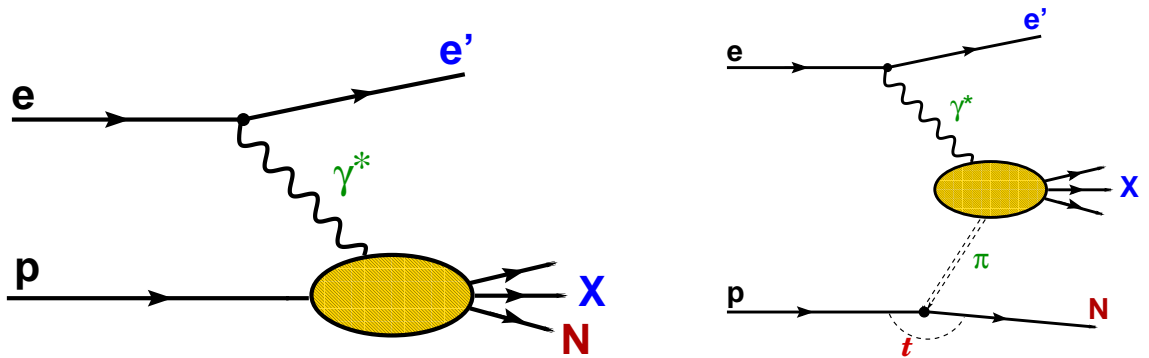


Fig. 15: (left) HERA  $ep$  scattering event with the final state baryon in the proton fragmentation system, (right) Leading baryon production via an exchange process.

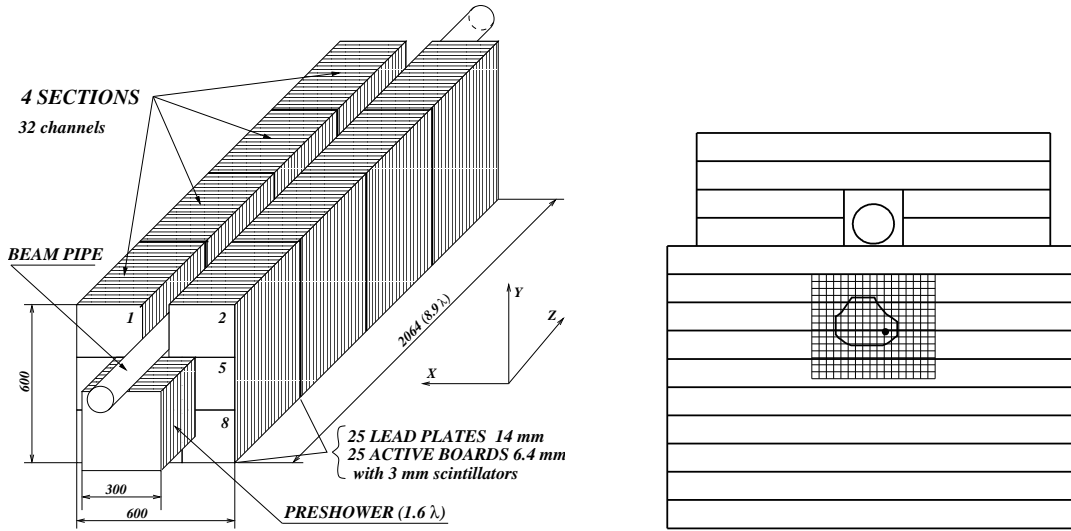


Fig. 16: General view of the H1-FNC calorimeter (left) and ZEUS-FNC calorimeter (right).

is  $\sim 2$ mm. Apart from improvement of the energy and position resolution the Preshower provides efficient separation of electromagnetic and hadronic showers. The Main Calorimeter of H1-FNC is a sandwich-type calorimeter consisting of four identical sections with transverse dimensions  $60 \times 60 \text{ cm}^2$  and length of 51.5 cm. Each section consists of 25 lead absorber plates 14 mm-thick, and 25 active boards with 3 mm scintillators. Each active board is made of 8 scintillating tiles with the transverse size of  $20 \times 20 \text{ cm}$  or  $20 \times 26 \text{ cm}$ . The 25 tiles of one section with the same transverse position form a “tower”. All together there are 32 towers in all four sections. In the top part of the calorimeter there is an opening for the proton beam vacuum pipe which is going through the calorimeter as seen from Fig. 16. The total length of the Main FNC calorimeter is 206.5 cm.

The structure of the ZEUS-FNC calorimeter is shown in Fig. 16(right). It is a finely segmented, compensating, sampling calorimeter with 134 layers of 1.25cm-thick lead plates as absorber and 2.6mm-thick scintillator plates as the active material. The scintillator is read out on each side with wavelength-shifting light guides coupled to photomultiplier tubes. It is segmented longitudinally into a front section, seven interaction-lengths deep, and a rear section, three interaction-lengths deep. The front section is divided vertically into 14 towers, each 5cm high. Inside the calorimeter at a depth of one interaction length a forward neutron tracker (FNT) is installed. It is a scintillator hodoscope designed to measure the position of neutron showers. Each scintillator finger is 16.8cm long, 1.2cm wide and 0.5cm deep; 17 are used for  $X$  position reconstruction and 15 for  $Y$ . The position of the FNT hodoscope in the FNC is indicated in Fig. 16.

The acceptance of the FNC calorimeters is defined by the aperture of the HERA beam line magnets and is limited to neutron scattering angles of  $\theta_n < 0.8 \text{ mrad}$  with approximately 30% azimuthal coverage (see Fig. 17). Thus the transverse momenta of neutrons are limited to  $p_{T,n}^{max} = 0.656 \cdot x_L$  for proton beam energy of 920 GeV. The overall acceptance of the FNC,



taking account of beam-line geometry, inactive material, beam tilt and angular spread, as well as the angular distribution of the neutrons, is  $\sim 20\%$  at low  $x_L$ , where the  $p_{T,n}$  range covered is small, but increases monotonically, exceeding 30% at high  $x_L$ .

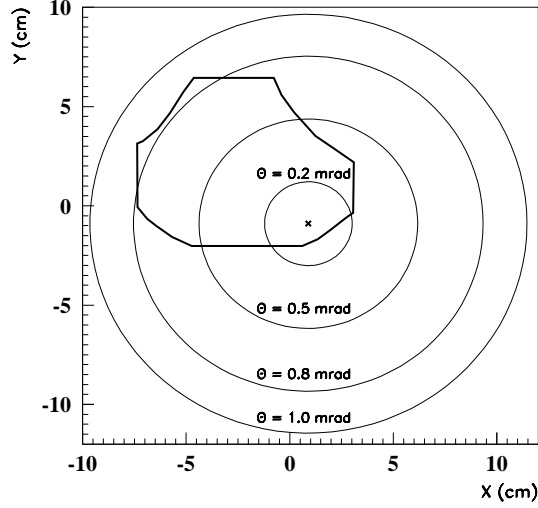


Fig. 17: The geometrical acceptance of FNC calorimeter defined by the aperture of the HERA beam-line elements.

**Physics with Leading Neutrons** The main goal of the FNC calorimeters is to measure the energy and angles of fast neutrons from the reaction  $ep \rightarrow e' + X + n$  (see Fig. 15). The H1 and ZEUS Collaborations provided many results on leading neutron production in DIS, photoproduction, in events containing jets or charm in the final state [32]. The results are successfully interpreted within the approach that at high  $x_L = E_n/E_p$  and low  $p_{T,n}$  the dominant mechanism of forward neutron production is the  $\pi^+$ -exchange.

An example of the observed neutron energy and the transverse momentum distributions for the deep-inelastic scattering (DIS) events is shown in Fig. 18 and compared with the Monte Carlo simulation [33]. The distribution is well described by the pion exchange Monte Carlo simulation (RAPGAP) with some admixture of the standard DIS Monte Carlo simulation (DJANGO).

Based on the assumption that at high  $x_L$  the leading neutron production is dominated by the pion exchange mechanism, the measurement of DIS cross sections in events with leading neutrons can provide an important information about the pion structure. The quark and gluon distributions of the pion have previously been constrained using Drell–Yan data and direct photon production data obtained by  $\pi p$  scattering experiments and are limited to high  $x$  ( $x > 0.1$ ) values. Figure 19 shows  $F_2^{LN(3)}/\Gamma_\pi$  as a function of  $\beta$  for fixed values of  $Q^2$ . Here,  $F_2^{LN(3)}$  is the measured semi-inclusive structure function for leading neutron production,  $\Gamma_\pi$  is the integrated pion flux, and  $\beta = x/(1-x_L)$  is a Bjorken scaling variable for the virtual pion. Thus,  $F_2^{LN(3)}/\Gamma_\pi$  can be interpreted as a pion structure function  $F_2^\pi$  and can distinguish between the different parameterisations of the pion structure function (Fig. 19). Moreover, using the measured rate

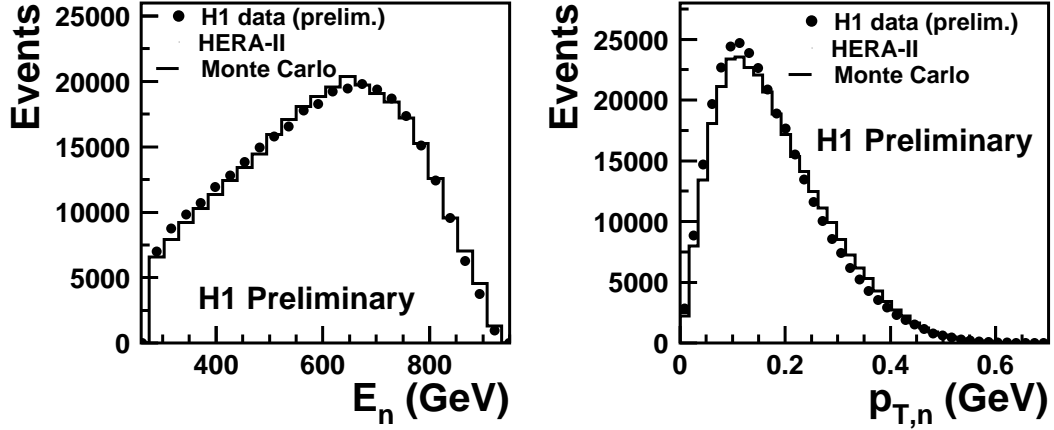


Fig. 18: The observed neutron energy spectrum and the transverse momentum  $p_T$  distribution from the DIS interactions. The data distribution is compared with the Monte Carlo simulation, which is the mixture of RAPGAP with pion exchange and the DJANGO models.

of leading neutron production in DIS, the total probability of  $p \rightarrow n\pi^+$  fluctuation in DIS of 16–25% was estimated [34].

In exchange models, neutron absorption can occur through rescattering. Absorption is a key ingredient in calculations of gap-survival probability in  $pp$  interactions at the LHC, critical in interpreting hard diffractive processes, including central exclusive Higgs production. In the processes with leading neutron production, due to the rescattering the neutron may migrate to lower  $x_L$  and higher  $p_T$  such that it is outside of the detector acceptance. The rescattering can also transform the neutron into a charged baryon which may also escape detection. Since the size of the virtual photon is inversely related to  $Q^2$ , more neutron rescattering would be expected for photoproduction ( $Q^2 \approx 0$ ) than for deep inelastic scattering. The size of the  $n\text{-}\pi$  system is inversely proportional to the neutron  $p_T$ , so rescattering removes neutrons with large  $p_T$ . Thus rescattering results in a depletion of high  $p_T$  neutrons in photoproduction relative to DIS: a violation of vertex factorization. Figure 20 shows the ratio of the  $x_L$  distributions for photoproduction and DIS. In the range  $0.2 < x_L < 0.4$ , the ratio drops slightly but rises for higher  $x_L$  values, exceeding unity for  $x_L > 0.9$ . The deviation of the ratio from unity is a clear violation of vertex factorization. The dashed and solid curves in Fig. 20 are the expectation for the suppression of leading neutrons in photoproduction relative to DIS from a model of pion exchange with neutron absorption [35]. Within the normalization uncertainty the data are well described by the absorption model. Also shown in Fig. 20 is another model [36] which employs the optical theorem together with multi-Pomeron exchanges to describe all possible rescattering processes of the leading hadron, resulting in absorptive effects. With the correction for different  $W$  dependences, the prediction is close in magnitude to the data.

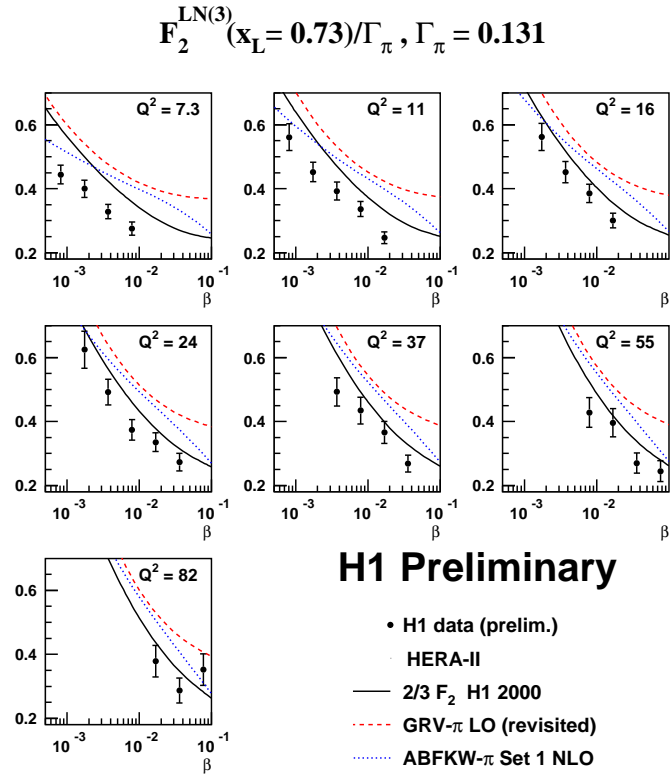


Fig. 19:  $F_2^{LN(3)}/\Gamma_\pi$  at  $x_L = 0.73$  plotted as a function of  $\beta$  for fixed values of  $Q^2$ . The quantity  $\Gamma_\pi$  is the  $p_T$  integrated pion flux factor.

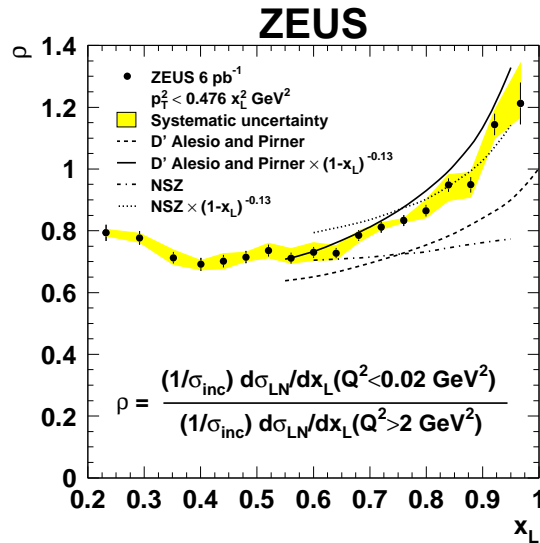


Fig. 20: Ratio of photoproduction and DIS  $x_L$  distributions, compared to the different rescattering models (see text)

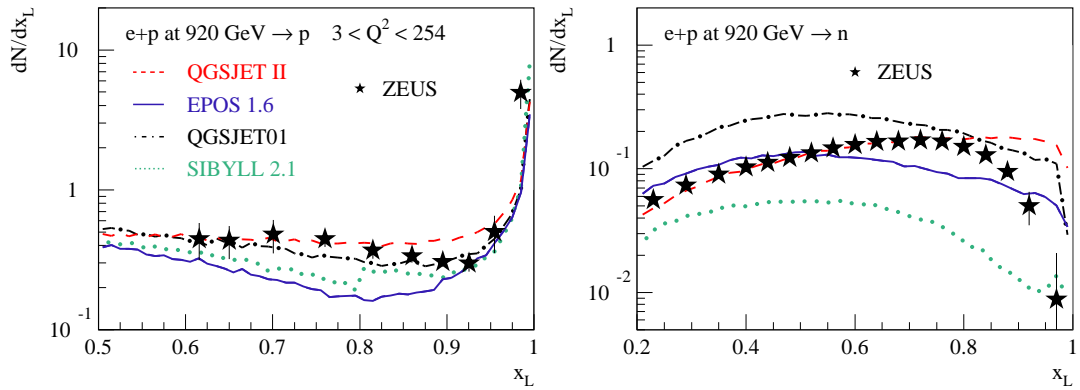


Fig. 21: Comparison of the leading proton and the leading neutron spectra measured at HERA (ZEUS [37]) with the predictions of the models used for cosmic ray analyses.

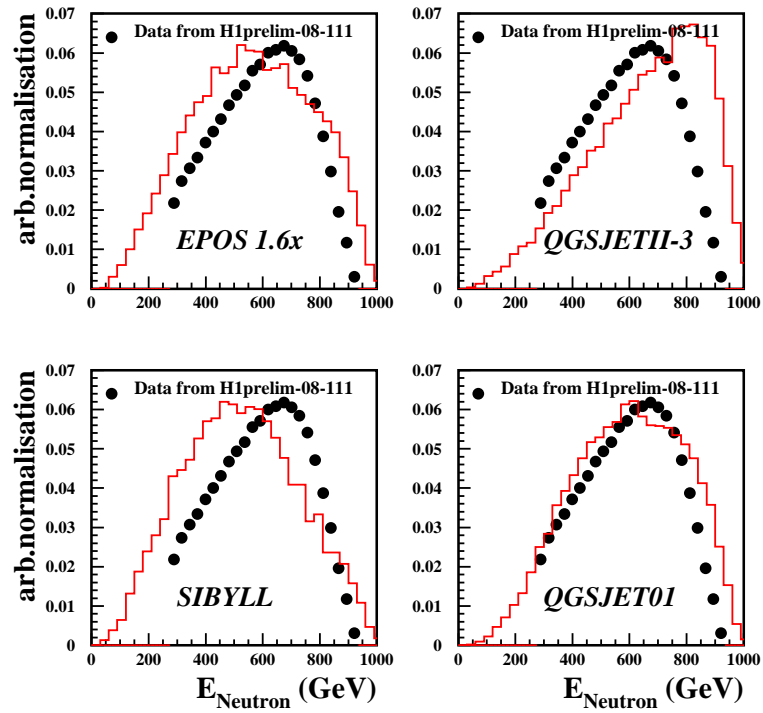


Fig. 22: Comparison of the leading neutron energy spectra measured at HERA (H1 [33]) with the predictions of the models used for cosmic ray analyses. The distributions are normalised to compare the shapes.

**Forward Particles at HERA and Cosmic Rays** The measurements of forward particles at HERA may provide valuable information for the physics of ultra-high energy cosmic rays. Despite the huge difference between the energy ranges accessible in the cosmic rays and the colliders, we may assume that the hadron production in the proton fragmentation region doesn't depend much on the energy and the type of interacting particle. The longitudinal segmentation of the FNC calorimeters at HERA allows to separate signals from the neutrons from that of photons, thus the experiments can measure the differential distributions of  $x_L$  and  $p_T$  for the neutrons and the photons. Moreover, the measurements can be made also for the different proton beam energies (we recall that the last three months the HERA collider was running at lower proton beam energies). The cosmic ray models can make predictions for these measurements and be tuned accordingly.

Comparison of the leading proton and the leading neutron spectra measured at HERA with the predictions of the models used for cosmic ray analyses are shown in Figs. 21 and 22. Here, the comparison is made before the detailed tunings of the models. It demonstrates that the HERA measurements are indeed sensitive to the differences between the models and can be used for the tuning of model parameters.

To summarise, the HERA experiments provide a wealth of measurements of leading baryon production. These measurements give an important input for an improved theoretical understanding of the proton fragmentation mechanism. The HERA data on forward particle production can help to reduce the uncertainty in the model predictions for very high energy cosmic ray air showers.

**Forward Particles at LHC** At the LHC, the collision energy of protons,  $\sqrt{s}=14$  TeV, corresponds to  $10^{17}$  eV in the laboratory system. So the measurements at the LHC are important to constrain the interaction models used in the cosmic-ray studies. The LHC is also capable of colliding different kind of ions. Measurements of ion collisions especially to simulate the interactions between cosmic-rays and atmosphere are also valuable. In the collider experiments, most of the collision energy flows into the very forward direction that is not covered by the general purpose detectors like ATLAS and CMS in case of the LHC. Dedicated experiments to cover these high rapidity region are necessary for the cosmic-ray studies. Fig. 23 shows the energy flux in 14 TeV collisions as a function of pseudo-rapidity  $\eta$ . Two independent experiments LHCf, TOTEM, and sub-detectors of the big experiments ZDCs are capable of measuring very forward particles. Coverage of each experiment in pseudo-rapidity is also indicated in Fig. 23 by arrows. Because each experiment has different capability (charged or neutral particle measurement, hadron or electromagnetic calorimeter, calorimeter or tracker, infinite or finite pseudo-rapidity coverage, aperture, position/energy resolutions), they provide complementary data for total understanding of the very forward particles.

LHCf (LHC forward) is an experiment dedicated to solve the cosmic-ray problems [38]. The experiment is a kind of ZDC (Zero Degree Calorimeter) but optimized to discriminate the interaction models used in the cosmic-ray studies. In LHC, at 140 m away from IP1 the beam pipe makes a transition from a common beam pipe facing the IP to two separate beam pipes joining to the arcs of LHC (the Y vacuum chamber). LHCf has installed two detectors in this 96 mm gap between two pipes at either side of IP1 and will measure the neutral particles of

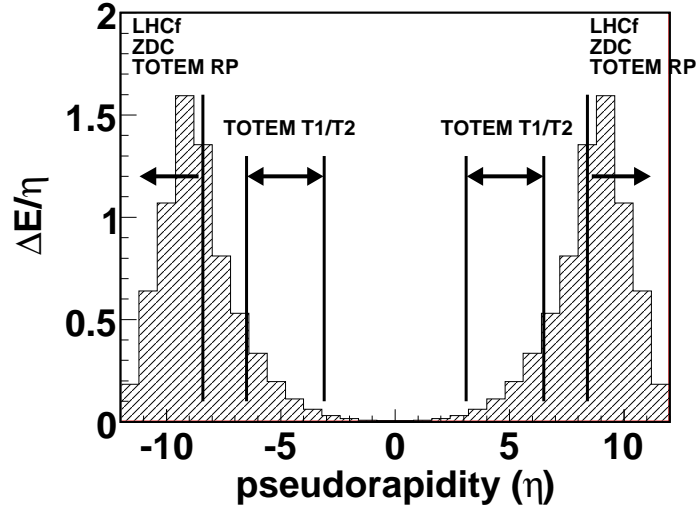


Fig. 23: pseudo-rapidity distribution at LHC

$\eta > 8.4$ . Each detector has two sampling calorimeter towers with  $44 X_0$  made of plastic scintillators and tungsten. The transverse cross-section of the calorimeters ranges from  $20 \text{ mm} \times 20 \text{ mm}$  to  $40 \text{ mm} \times 40 \text{ mm}$ . One detector has Scifi and MAPMT, and the other has silicon strip tracker for position measurements. The detectors can measure the energy and  $P_T$  distributions of gamma-rays and neutrons. Small double-tower configuration enables analysis of  $\pi^0$  mass reconstruction by measuring the energies and positions of decayed gamma-ray pairs, consequently the determination of the  $\pi^0$  energy spectrum. With the energy resolution better than 5% for gamma-rays and 30% for hadrons, and position resolution better than 0.2 mm, major models used in the CR studies can be discriminated as shown in Fig. 24. A comparison study considering some recent models has also predicted large variation from model to model that can be confirmed by the LHCf measurements [39]. LHCf can also study the Landau-Pomeranchuk-Migdal (LPM) effect in detail. In the tungsten calorimeter, electromagnetic showers of  $> \text{TeV}$  energy show  $> 10\%$  deviation from the non-LPM expectation. LHCf is planning to take data in the early stage of the LHC commissioning.

TOTEM is an experiment to measure the total cross section in the proton collisions at IP5 in the LHC [38]. TOTEM measures the numbers of the proton elastic scattering using the Roman Pot detectors and inelastic scattering using the so-called telescopes surrounding the beam pipe. The RP detectors also measure the position of the elastically scattered protons to determine  $dN_{el}/dt$  at  $t=0$  extrapolation. Combining these measurements and the optical theorem, TOTEM will determine the total cross section with  $\pm 1 \text{ mb}$  error.

ZDCs are the sub detectors of the ATLAS, CMS and ALICE experiments. Except a part of the ALICE ZDC (ZP), all ZDCs are installed in the place where the beam pipe is separated into two as was the case of LHCf. The prime motivation of the ZDCs is to determine the energy

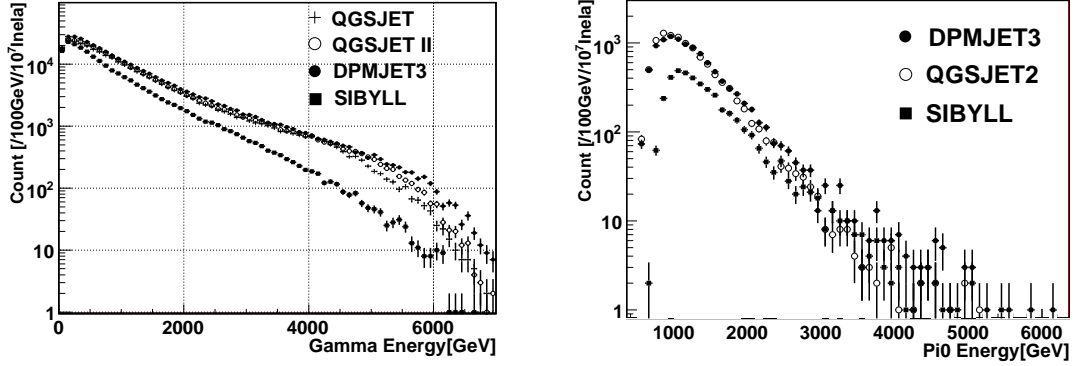


Fig. 24: Energy spectra of single  $\gamma$ -rays and  $\pi^0$ 's expected in the LHCf measurement using different interaction models.

carried by the spectator nucleons in ion collisions. For this purpose, ZDCs have as wide aperture as possible in the limited volume and as thick material as possible to measure the energy flow of the nucleons.

In summary, the LHC gives an unprecedented opportunity to constrain the interaction models used in the cosmic-ray studies. The integration of the data from not only the experiment dedicated for the cosmic-ray science (LHCf) but also the others, especially the forward experiments introduced above is important to constrain the interaction models used in the cosmic-ray studies.

### 3 Neutrino cross section and uncertainties

Predictions of neutrino cross-sections at high energies have sizeable uncertainties which derive largely from the measurement uncertainties on the parton distribution functions (PDFs) of the nucleon. In the framework of the quark-parton model, high energy scattering accesses very large values of  $Q^2$ , the invariant mass of the exchanged vector boson, and very small values of Bjorken  $x$ , the fraction of the momentum of the incoming nucleon taken by the struck quark. Thus when evaluating uncertainties on high energy neutrino cross-sections it is important to use the most up to date information from the experiments at HERA, which have accessed the lowest- $x$  and highest  $Q^2$  scales to date. The present paper outlines the use of the ZEUS-S global PDF fit formalism [40], updated to include *all* the HERA-I data. Full details are given in [41].

Conventional PDF fits use the Next-to-leading-order (NLO) Dokshitzer-Gribov-Lipatov-Altarelli-Parisi (DGLAP) formalism of QCD to make predictions for deep inelastic scattering (DIS) cross-sections of leptons on hadrons. At low- $x$  where the gluon density is rising rapidly it is probably necessary to go beyond the DGLAP formalism in order to resum  $\ln(1/x)$  diagrams, or even to consider non-linear terms which describe gluon recombination. Such approaches are beyond the scope of the present discussion, which is concerned with the more modest goal of estimating the uncertainties on high energy neutrino cross-sections which are compatible with

the conventional NLO DGLAP formalism. As a corollary, if cross-sections much outside the uncertainty bands presented here are observed, it would be a clear signal of the need for extensions to conventional formalism.

This work provide an update on the neutrino cross-sections in the literature [42] which used PDF sets which no longer fit modern data from HERA and an *ad hoc* procedure for estimating PDF uncertainties. There are several improvements on previous work. Firstly, a recent PDF analysis which includes data from all HERA-I running [40] is used. Secondly, a consistent approach to PDF uncertainties – both model uncertainties and, more importantly, the uncertainties which derive from the correlated systematic errors of the input data sets is used. Thirdly, NLO rather than LO calculations are used throughout. Fourthly, a general-mass variable flavour number scheme [43] is used to treat heavy quark thresholds.

The PDF fit formalism of the published ZEUS-S global PDF analysis [40] is used, but this fit is updated as follows. First, the range of the calculation has been extended up to  $Q^2 = 10^{12} \text{ GeV}^2$  and down to  $x = 10^{-12}$ . Second, *all* inclusive cross-section data for neutral and charged current reactions from ZEUS HERA-I running (1994–2000) are included in the fit. Third, the parametrization is extended from 11 to 13 free parameters, input at  $Q_0^2 = 7 \text{ GeV}^2$ .

The most significant source of uncertainties on the PDFs comes from the experimental uncertainties on the input data. The PDFs are presented with full accounting for uncertainties from correlated systematic errors (as well as from statistical and uncorrelated sources) using the conservative OFFSET method. The uncertainty bands should be regarded as 68% confidence limits. The PDF central values and uncertainties from this updated ZEUS-S-13 fit are comparable to those on the published ZEUS-S fit [40], as well as the most recent fits of the CTEQ [44] and MRST [45] groups.

Previous work [42] treated heavy quark production by using a zero-mass variable flavour number scheme, with slow-rescaling at the  $b$  to  $t$  threshold. The exact treatment of the  $b \rightarrow t$  threshold is not very important for the estimation of high energy neutrino cross-sections since the contribution of the  $b$  is suppressed, but the correct treatment of heavy quark thresholds is important in determining the PDFs for lower  $Q^2$  ( $\lesssim 5000 \text{ GeV}^2$ ) and middling  $x$  ( $5 \times 10^{-5} \lesssim x \lesssim 5 \times 10^{-2}$ ) and this is a kinematic region of relevance to the present study.

The results of this study show that the PDF uncertainty on the neutrino (and antineutrino) charged current (CC) cross-sections remains modest ( $< 15\%$ ) even at the highest energies considered here:  $s = 10^{12} \text{ GeV}^2$ . The reason for this is that the high energy ( $E_\nu > 10^7 \text{ GeV}$ )  $\nu N$  and  $\bar{\nu} N$  cross-sections are dominated by sea quarks produced by gluon splitting  $g \rightarrow q\bar{q}$  and, although the PDF uncertainty on the sea quarks is large at low- $x$  and low  $Q^2$ , the dominant contributions to the cross-sections do *not* come from very low  $Q^2$  values. The dominant contributions come from the kinematic region  $50 \lesssim Q^2 \lesssim 10^4 \text{ GeV}^2$  (where the exact region moves up gradually with  $s$ ). The contribution of higher  $Q^2$  ( $Q^2 > M_W^2$ ) is suppressed by the  $W$ -propagator. Furthermore, there is a restriction on the lowest value of  $x$  probed for each  $Q^2$  value due to the kinematic cut-off ( $y < 1$  and since  $x = Q^2/sy$ , we must have,  $x > Q^2/s$ ). This kinematic cut-off ensures that higher  $Q^2$  values do not probe very low- $x$  until the neutrino energies are very high indeed. For example, at  $E_\nu = 1.9 \times 10^7 \text{ GeV}$ , the important range is  $10^{-6} \lesssim x \lesssim 10^{-3}$ , while for  $E_\nu = 5.3 \times 10^9 \text{ GeV}$ , this moves down to  $10^{-8} \lesssim x \lesssim 10^{-4}$ . Full details on the PDF uncertainties and the predictions for the neutrino and antineutrino double



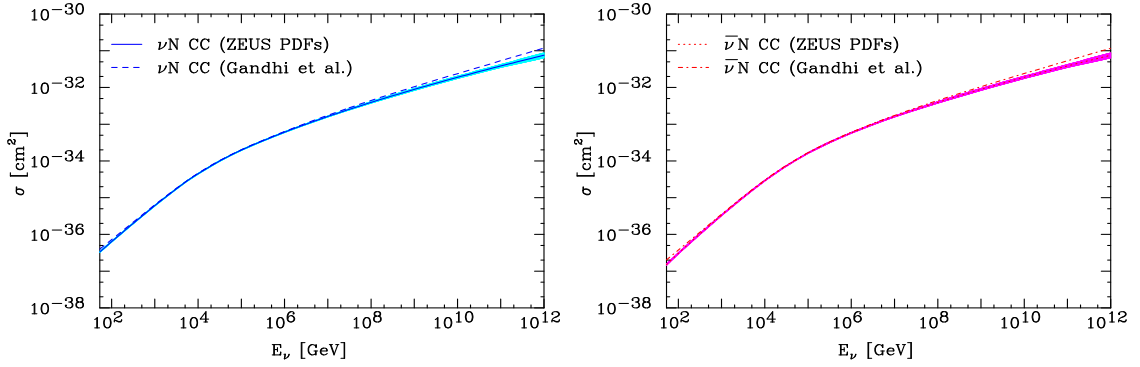


Fig. 25: The total CC cross-section at ultra high energies for neutrinos (left) and antineutrinos (right) along with the  $\pm 1\sigma$  uncertainties (shaded band), compared with the previous calculation by Gandhi *et al.*

differential cross-sections are given in reference [41].

The total CC cross-sections are obtained by integrating the predicted double differential cross-sections  $d^2\sigma/dx dy$ . These cross-sections are illustrated in Fig. 25 together with their uncertainties due to the PDFs, including both model uncertainties and the experimental uncertainties of the input data sets. The trend of the PDF uncertainties at high neutrino energy can be understood by noting that as one moves to higher and higher neutrino energies one also moves to lower and lower  $x$  where the PDF uncertainties are increasing. At lower neutrino energies ( $10^2 < E_\nu < 10^7$  GeV) the high- $x$  region becomes important and the neutrino and antineutrino cross-sections are *different* due to the valence PDF contribution. The onset of the linear dependence of the cross-section on  $s$  for  $s < M_W^2$  can be seen. The trend of the PDF uncertainties in the low energy region can be understood as follows: as one moves to lower neutrino energies one moves out of the very low- $x$  region such that PDF uncertainties decrease. These uncertainties are smallest at  $10^{-2} \lesssim x \lesssim 10^{-1}$ , corresponding to  $s \sim 10^5$ . Moving to yet lower neutrino energies brings us into the high- $x$  region where PDF uncertainties are larger again.

Figure 25 also compares our CC cross-section to the widely used leading-order calculation of Gandhi *et al* [42]. The present results show a less steep rise of the cross-section at high energies, reflecting the fact that more recent HERA cross-section data display a less dramatic rise at low- $x$  than the early data.

In conclusion, the charged current neutrino cross-section at NLO have been calculated in the Standard Model using the best available DIS data along with a careful estimate of the associated uncertainties. if cross-sections much outside the uncertainty bands presented here are observed at UHE cosmic neutrino detectors, it would be a clear signal of the need for extensions to conventional QCD DGLAP formalism.

## References

- [1] H1 Collaboration, I. Abt *et al.*, Nucl. Instrum. Meth. **A386**, 310 (1997).

- [2] ZEUS Collaboration, U. e. ZEUS-Collab., Holm, Status Report (unpublished), <http://www-zeus.desy.de/bluebook/bluebook.html> (1993).
- [3] P. D. B. Collins. Cambridge 1977, 445p.
- [4] V. N. Gribov, V. M. Shekhter, V. A. Kolkunov, and L. B. Okun, Sov. Phys. JETP **14**, 1308 (1962).
- [5] H1 Collaboration, S. Aid *et al.*, Z. Phys. **C69**, 27 (1995), arXiv:hep-ex/9509001.
- [6] ZEUS Collaboration, S. Chekanov *et al.*, Nucl. Phys. **B627**, 3 (2002), arXiv:hep-ex/0202034.
- [7] D. O. Caldwell *et al.*, Phys. Rev. Lett. **40**, 1222 (1978);  
HERA and COMPAS Groups Collaboration, S. I. Alekhin *et al.* CERN-HERA-87-01.
- [8] A. Donnachie and P. V. Landshoff, Phys. Lett. **B437**, 408 (1998), arXiv:hep-ph/9806344.
- [9] J. C. Collins and D. E. Soper, Ann. Rev. Nucl. Part. Sci. **37**, 383 (1987).
- [10] F. Halzen and A. D. Martin. New York, Usa: Wiley ( 1984) 396p.
- [11] V. N. Gribov and L. N. Lipatov, Sov. J. Nucl. Phys. **15**, 438 (1972);  
G. Altarelli and G. Parisi, Nucl. Phys. **B126**, 298 (1977);  
Y. L. Dokshitzer, Sov. Phys. JETP **46**, 641 (1977).
- [12] H. Collaboration, Preliminary Result H1prelim 07-007 (2007);  
Z. Collaboration, Preliminary Result ZEUS-prel 07-026 (2007).
- [13] H. Collaboration, Preliminary Result H1prelim 08-045 (2008);  
Z. Collaboration, Preliminary Result ZEUS-prel 08-003 (2008).
- [14] S. D. Ellis and D. E. Soper, Phys. Rev. **D48**, 3160 (1993), arXiv:hep-ph/9305266.
- [15] ZEUS Collaboration, S. Chekanov *et al.*, Nucl. Phys. **B765**, 1 (2007), arXiv:hep-ex/0608048.
- [16] H1 Collaboration, C. Adloff *et al.*, Eur. Phys. J. **C13**, 609 (2000), arXiv:hep-ex/9908059;  
ZEUS Collaboration, S. Chekanov *et al.*, Eur. Phys. J. **C21**, 443 (2001), arXiv:hep-ex/0105090.
- [17] E. A. Kuraev, L. N. Lipatov, and V. S. Fadin, Sov. Phys. JETP **44**, 443 (1976);  
I. I. Balitsky and L. N. Lipatov, Sov. J. Nucl. Phys. **28**, 822 (1978).
- [18] ZEUS Collaboration, S. Chekanov *et al.*, Eur. Phys. J. **C52**, 515 (2007), arXiv:0707.3093 [hep-ex].

- [19] H1 Collaboration, A. Aktas *et al.*, Eur. Phys. J. **C46**, 27 (2006), arXiv:hep-ex/0508055.
- [20] S. Catani and M. H. Seymour, Nucl. Phys. **B485**, 291 (1997), arXiv:hep-ph/9605323.
- [21] H. Jung and G. P. Salam, Eur. Phys. J. **C19**, 351 (2001), arXiv:hep-ph/0012143; H. Jung, Comput. Phys. Commun. **143**, 100 (2002), arXiv:hep-ph/0109102.
- [22] M. Ciafaloni, Nucl. Phys. **B296**, 49 (1988); S. Catani, F. Fiorani, and G. Marchesini, Nucl. Phys. **B336**, 18 (1990).
- [23] H. Jung, Comp. Phys. Commun. **86**, 147 (1995).
- [24] L. Lonnblad, Comput. Phys. Commun. **71**, 15 (1992).
- [25] H. Collaboration, Preliminary Result H1prelim 07-132 (2007); Z. Collaboration, Preliminary Result ZEUS-prel 07-025 (2007).
- [26] H. Collaboration, Preliminary Result H1prelim 08-031 (2008).
- [27] Z. Fodor, S. D. Katz, A. Ringwald, and H. Tu, Phys. Lett. **B561**, 191 (2003), arXiv:hep-ph/0303080.
- [28] HiRes Collaboration, R. Abbasi *et al.*, Phys. Rev. Lett. **100**, 101101 (2008), arXiv:astro-ph/0703099.
- [29] K.-H. Kampert, J. Phys. Conf. Ser. **120**, 062002 (2008), arXiv:0801.1986 [astro-ph].
- [30] H1 Collaboration, C. Adloff *et al.*, Eur. Phys. J. **C25**, 495 (2002), arXiv:hep-ex/0205078; ZEUS Collaboration, S. Chekanov *et al.*, Eur. Phys. J. **C34**, 255 (2004), arXiv:hep-ex/0312048.
- [31] J. D. Sullivan, Phys. Rev. **D5**, 1732 (1972); H. Holtmann, G. Levman, N. N. Nikolaev, A. Szczurek, and J. Speth, Phys. Lett. **B338**, 363 (1994); B. Kopeliovich, B. Povh, and I. Potashnikova, Z. Phys. **C73**, 125 (1996), arXiv:hep-ph/9601291; M. Przybycien, A. Szczurek, and G. Ingelman, Z. Phys. **C74**, 509 (1997), arXiv:hep-ph/9606294; A. Szczurek, N. Nikolaev, and J. Speth, Phys. Lett. **B428**, 383 (1998), arXiv:hep-ph/9712261.
- [32] H1 Collaboration, C. A. e. a. H1 Coll., Eur. Phys. J. **C6**, 587 (1999), arXiv:hep-ex/9811013; ZEUS Collaboration, J. B. e. a. ZEUS Coll., Nucl. Phys. **B596**, 3 (2001),

- arXiv:hep-ex/0010019;  
ZEUS Collaboration, S. C. e. a. ZEUS Coll., Nucl. Phys. **B637**, 3 (2002),  
arXiv:hep-ex/0205076;  
ZEUS Collaboration, S. C. e. a. ZEUS Coll., Phys. Lett. **B590**, 143 (2004),  
arXiv:hep-ex/0401017;  
ZEUS Collaboration, S. C. e. a. ZEUS Coll., Phys. Lett. **B610**, 199 (2005),  
arXiv:hep-ex/0404002;  
H1 Collaboration, A. A. e. a. H1 Coll., Eur. Phys. J. **C41**, 273 (2005),  
arXiv:hep-ex/0501074;  
ZEUS Collaboration, S. C. e. a. ZEUS Coll., Nucl. Phys. **B776**, 1 (2007),  
arXiv:hep-ex/0702028;  
F. A. e. a. H1 Coll., *Leading Neutron Production in DIS at HERA* . H1prelim-08-111,  
presented at ICHEP-08, Philadelphia, 2008.
- [33] H1 Collaboration, *Leading Neutron production in DIS at HERA* . H1-Preliminary-08-111,  
presented at ICHEP-2008, Philadelphia, 2008.
- [34] A. Bunyatyan and B. Povh, Eur. Phys. J. **A27**, 359 (2006), arXiv:hep-ph/0603235.
- [35] U. D'Alesio and H. J. Pirner, Eur. Phys. J. **A7**, 109 (2000), arXiv:hep-ph/9806321.
- [36] N. Nikolaev, J. Speth, and B. G. Zakharov, *Absorptive corrections to the one pion exchange and measurability of the small-x pion structure function at HERA*. Preprint KFA-IKP(TH)-1997-17, 1997. arXiv:hep-ph/9708290.
- [37] ZEUS Collaboration, S. C. e. a. ZEUS Coll., Nucl. Phys. **B658**, 3 (2003),  
arXiv:hep-ex/0210029.
- [38] LHCf Collaboration, O. Adriani *et al.*, JINST **3**, S08006 (2008).
- [39] H.-J. Drescher, Phys. Rev. **D77**, 056003 (2008), arXiv:0712.1517 [hep-ph].
- [40] ZEUS Collaboration, S. Chekanov *et al.*, Phys. Rev. **D67**, 012007 (2003),  
arXiv:hep-ex/0208023.
- [41] A. Cooper-Sarkar and S. Sarkar, JHEP **01**, 075 (2008), arXiv:0710.5303  
[hep-ph].
- [42] R. Gandhi, C. Quigg, M. H. Reno, and I. Sarcevic, Phys. Rev. **D58**, 093009 (1998),  
arXiv:hep-ph/9807264.
- [43] R. S. Thorne and R. G. Roberts, Phys. Rev. **D57**, 6871 (1998),  
arXiv:hep-ph/9709442;  
R. S. Thorne, Phys. Rev. **D73**, 054019 (2006), arXiv:hep-ph/0601245.
- [44] J. Pumplin *et al.*, JHEP **07**, 012 (2002), arXiv:hep-ph/0201195;  
W. K. Tung *et al.*, JHEP **02**, 053 (2007), arXiv:hep-ph/0611254.

- [45] A. D. Martin, R. G. Roberts, W. J. Stirling, and R. S. Thorne, *Eur. Phys. J.* **C23**, 73 (2002),  
arXiv:hep-ph/0110215;  
A. D. Martin, W. J. Stirling, R. S. Thorne, and G. Watt, *Phys. Lett.* **B652**, 292 (2007),  
arXiv:0706.0459 [hep-ph].